Something something something physics

Steven Green
of Emmanuel College

A dissertation submitted to the University of Cambridge
for the degree of Doctor of Philosophy

Abstract

This thesis describes the optimisation of the calorimeter design for collider experiments at the future Compact LInear Collider (CLIC) and the International Linear Collider (ILC). The detector design of these experiments is built around high-granularity Particle Flow Calorimetry that, in contrast to traditional calorimetry, uses the energy measurements for charged particles from the tracking detectors. This can only be realised if calorimetric energy deposits from charged particles can be separated from those of neutral particles. This is made possible with fine granularity calorimeters and sophisticated pattern recognition software, which is provided by the PandoraPFA algorithm. This thesis presents results on Particle Flow calorimetry performance for a number of detector configurations. To obtain these results a new calibration procedure was developed and applied to the detector simulation and reconstruction to ensure optimal performance was achieved for each detector configuration considered.

This thesis also describes the development of a software compensation technique that vastly improves the intrinsic energy resolution of a Particle Flow Calorimetry detector. This technique is implemented within the PandoraPFA framework and demonstrates the gains that can be made by fully exploiting the information provided by the fine granularity calorimeters envisaged at a future linear collider.

A study of the sensitivity of the CLIC experiment to anomalous gauge couplings that effect vector boson scattering processes is presented. These anomalous couplings provide insight into possible beyond standard model physics. This study, which utilises the excellent jet energy resolution from Particle Flow Calorimetry, was performed at centre-of-mass energies of 1.4 TeV and 3 TeV with integrated lumi-

nosities of 1.5ab^{-1} and 2ab^{-1} respectively. The precision achievable at CLIC is shown to be approximately one to two orders of magnitude better than that currently offered by the LHC.

Finally, a study into various technology options for the CLIC vertex detector is described.

Declaration

This dissertation is the result of my own work, except where explicit reference is made to the work of others, and has not been submitted for another qualification to this or any other university. This dissertation does not exceed the word limit for the respective Degree Committee.

Andy Buckley

Acknowledgements

Of the many people who deserve thanks, some are particularly prominent, such as my supervisor...

Preface

This thesis describes my research on various aspects of the LHCb particle physics program, centred around the LHCb detector and LHC accelerator at CERN in Geneva.

For this example, I'll just mention Chapter **??** and Chapter **??**.

x

Contents

*"Writing in English is the most ingenious torture
ever devised for sins committed in previous lives."*
— James Joyce

Chapter 1.

Capacitively Coupled Pixel Detectors for the CLIC Vertex Detector

"There, sir! that is the perfection of vessels!"
   — Jules Verne, 1828–1905

1.1. Introduction

Identification of heavy-flavour quarks and tau-leptons relies at the linear collider experiment will rely upon precise reconstruction of secondary displaced vertices that are produced when these particles decay. Furthermore, the ability to accurately associate any daughter tracks, which are produced from such decays, to the secondary vertices is essential. At the CLIC experiment this can only be realised using a vertex detector with a very high spatial resolution, of approximately 3 μm, and good geometric coverage, extending to low θ values. The vertex detector must also have a low material budget (less than 0.2 X_0 per layer) in order to prevent additional decay vertices from material interactions (CONFIRM!), and maintain a low occupancy, despite the high presence of beam-induced background particles. Low occupancy for the vertex detector will be achieved through the use of time-tagging, to an accuracy of 10 ns, to identify particles produced from the physics event of interest.

As there are currently no technology options that fulfil all of the criteria for the CLIC vertex detector, the CLIC experiment has developed an extensive R&D program where

new technologies for the vertex detector are considered. High-voltage complementary metal-oxide-semiconductor (HV-CMOS) sensors, which are capacitively coupled to a separate readout application-specific integrated circuit (ASIC) are one such option. The performance of prototype detectors based upon this technology and the impact of mechanical tolerances present in their manufacture are presented.

1.1.1. HV-CMOS

Pixel detectors can be broadly classified in two distinct groups: hybrid detectors, where a separate sensor and readout chip are bonded together; and fully-integrated devices, where the collection diode is implanted in the same piece of silicon as the readout circuitry. Fully-integrated devices have traditionally not been suitable for applications with tight timing requirements, due to relatively slow charge collection time and limited on-pixel functionality. However, recent developments in CMOS technologies, a method for constructing integrated circuits, have led to new assembly designs that may overcome some of these issues.

HV-CMOS is a processing technology whereby the n-MOS and p-MOS transistors forming the on-pixel electronics, are placed entirely within a deep n-well, as shown in 1.1. By varying the voltage applied at the gate terminal, n-MOS and p-MOS transistors are able to control the currently flowing between the source and drain terminals. The gate voltage produces an inversion layer between the source and drain terminals that acts as a conduit allowing current to flow between the source and drain, as shown in figure 1.2. The magnitude of the voltage at the gate, with respect to the body, controls the width of the inversion layer and henceforth the magnitude of this current. Logic operations can be performed directly on-pixel using various configurations of the n-MOS and p-MOS transistors.

For the HV-CMOS, the deep n-well housing the on-pixel electronics acts as the charge collection diode as well as shielding the circuitry from the p-substrate. This shielding allows for the application of a moderate bias voltage to the sensor bulk that produces a depletion region, which facilitates fast charge collection via a drift current. In contrast, traditional monolithic active pixel sensors (MAPS) have a much smaller depletion region meaning charge collection occurs primarily through the slower mechanism of diffusion. Furthermore, in conventional MAPS there is potential for competition for charge collection between the n-well collecting diode and the
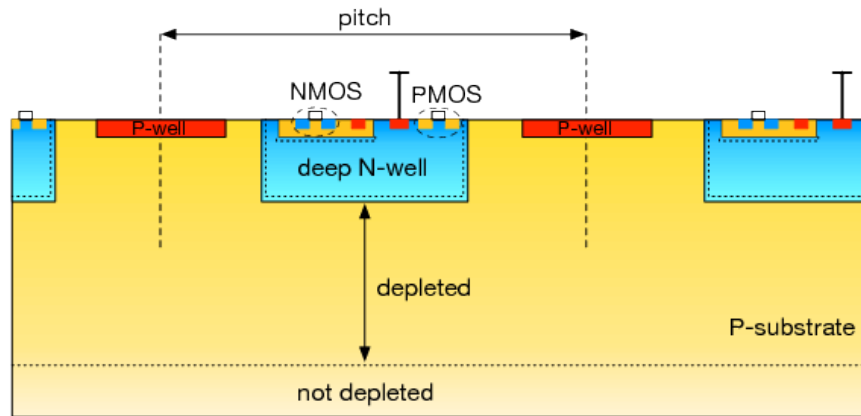
Figure 1.1.: Schematic cross section of an HV-CMOS sensor: the deep n-well is the charge-collecting electrode and also contains additional CMOS circuits such as a preamplifier. Image taken from [3].
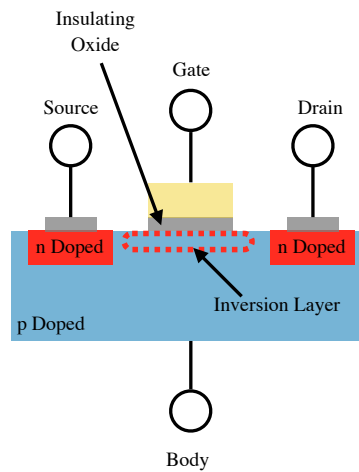

Figure 1.2.: Schematic cross section of an n-MOS transistor. p-MOS transistors have a similar cross section where the n and p doped regions are switched.

p-MOS transistors used to perform logic operations as the p-MOS transistors are embedded within an n-well. The HV-CMOS technology does not suffer from this effect as the deep n-well collecting diode houses the p-MOS transistors.

The HV-CMOS technology offers the possibility of fast charge collection with integrated on-pixel functionality, however, several limitations still exist. As the on-pixel electronics have to be placed inside the deep n-well and the n-wells have to be separated from each other, there is a limited physical area of the pixel that can be used for the transistor layout, which limits the available on-pixel functionality. In

addition to this, it is not possible to implement full CMOS logic inside the deep n-well as coupling between p-MOS transistors and the collection diode will lead to noise injection. While it is possible to embed p-MOS transistors within a p-well to shield them from the deep n-well, quadruple-well technology, and give access to full CMOS logic this option is not readily available for prototyping. By restricting the complexity of on-pixel electronics and using a separate readout ASIC, it is possible to overcome many of these issues. When coupled with the fast charge collection time and removal of competition in charge collection this makes the HV-CMOS technology option highly desirable for use in the CLIC vertex detector.

1.1.2. CLIC ASICs

As the HV-CMOS technology is such a promising option for use at the CLIC vertex detector, prototype devices based on this technology have been developed for testing. Two ASICs have been developed: the charge coupled pixel device version 3 (CCPDv3), a sensor chip based on the HV-CMOS technology, and the CLICpix, a readout chip providing additional on-pixel logic operations. The pitch of the sensors, both the CCPDv3 and the CLICpix, produced for this study is 25 μm, which should be sufficient to meet the requirements for the CLIC vertex detector and the matrix size is 64×64. A schematic of these devices can be found in figure 1.3.
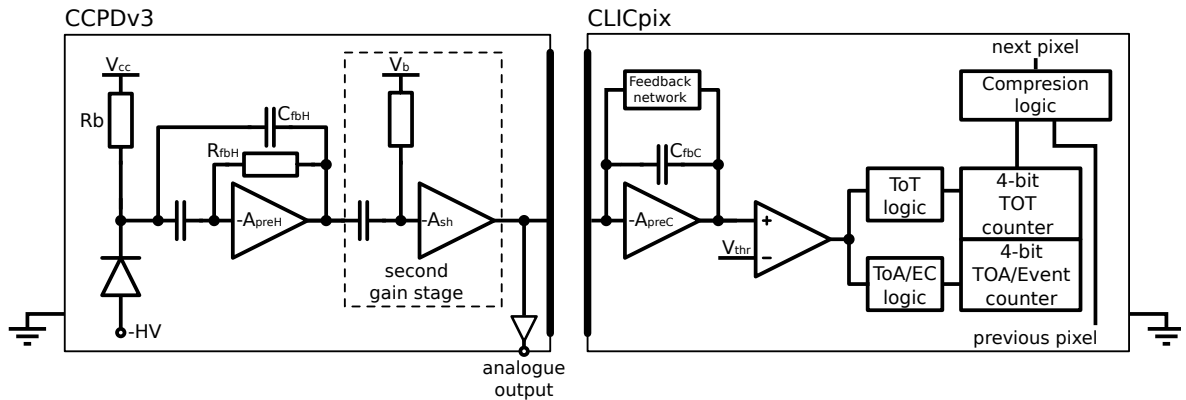

Figure 1.3.: Schematic of CCPDv3 and CLICpix pixels.

CCPDv3

The construction of the CCPDv3 was done using a 65nm CMOS process, which is the smallest size building blocks that can be used for creating the integrated circuits on a silicon wafer. This pushes the boundaries of semiconductor device fabrication for particle collider pixel detectors as current LHC experiments typically use 130 and/or 250 nm CMOS processes in the pixel detectors [1,5]. This makes it possible to have more complex on-pixel circuitry incorporated into the CLIC vertex detector than would be possible in previous generations of pixel detectors.

CLICpix

The CLICpix is a hybrid pixel readout chip that has been developed for the CLIC vertex detector. Each CLICpix pixel contains a charge-integrating amplifier connected to a discriminator, as shown in figure 1.3. The discriminator fires for as long as the input signal is over a given threshold and this output is then used as the input for further logic operations. The additional logic operations record the time of arrival and magnitude of the collected charge, using a Time over Threshold (ToT) measurement. The ToT is stored in a 4-bit on-pixel counter. The CLICpix operates using a shutter-based readout, where the entire matrix is kept active while the shutter is open and when closed the matrix is readout in its entirety. This is designed in order to match the expected beam structure for the CLIC experiment, as the accelerator will deliver bunch trains of e^+ and e^- that are separated by 20 ms. Each bunch train contains 312 bunches with a spacing of 0.5 ns, giving a total train length of 156 ns. Furthermore, the shutter-based readout is well suited to power-pulsing, whereby, the power to front-end electronics is turned off between bunch crossings. This helps to significantly reduce the power consumption of the pixel detector.

The threshold voltage seen by each CLICpix pixel is slightly different, due to variations in the manufacturing process. If these variations are not accounted for then the behaviour of the device across the matrix will not be uniform. To minimise the impact of these fluctuations each CLICpix pixel contains a 4-bit local adjustment to the threshold voltage, which is calibrated to unify the response across the matrix. The threshold 'equalisation' is achieved by performing two threshold scans across the matrix, once with all four bits set to 0 (no local threshold adjustment), and a second time with all four bits set to 1 (maximum local threshold adjustment). For each scan,

the baseline voltage of each pixel is determined. By applying a linear interpolation between the 0000 and 1111 cases, each pixel can be tuned to a common point, such that all pixels respond at the same global threshold.

1.1.3. Capacitive Coupling

Solder bump-bonding is the typical method used to connect sensor and readout ASICs in hybrid pixel detectors, however, it is expensive and sets limits on the thickness of both ASICs that is required for mechanical stability. An alternative procedure for connecting the ASICs involves using a thin layer of glue to form a capacitive connection between the two. This procedure reduces the cost and material budget with respect to bump-bonding making it highly desirable for use at the CLIC vertex detector. However, as this procedure has only recently been used to produce prototype devices extensive tests have to be performed to determine whether this option is feasible. In order to make this procedure viable it is necessary to implement an amplifier in the CCPDv3 on-pixel logic, shown in figure 1.3, to boost the signal to overcome the intrinsically small capacitance of the gluing layer.

1.2. Construction

Two of the main issues involved in constructing capacitively coupled pixel detectors are the uniformity of the glue layer achieved and the physical alignment between the pads on the active sensor and the readout ASIC. While the former has been investigated in another study (CITE STUDY), the latter will be presented below. For this work, a number of pixel detectors were constructed that contained misalignments between the HV-CMOS and CLICpix coupling pads (as shown in figure 1.4), in order to quantify the impact on the detector performance. Table 1.1 contains a summary of the samples studied.

The full details of the glueing process can be found in [CERN NOTE CITE], along with a study of the absolute precision of the manufacturing procedure. It was found that for devices constructed in an identical fashion to those considered here, the glue layer thicknesses were less than 1 μm and the precision on the pad positioning was less than 0.5 μm.
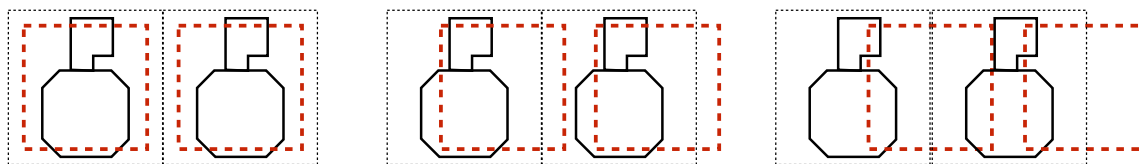
Figure 1.4.: Alignment schematic of the CCPDv3 + CLICpix detectors studied. The red dotted line represents the CCPDv3 pad and the solid black line represents the CLICpix top metal layer. From left to right; centred pixels, 1/4 offset (6.25 μm) and 1/2 offset (12.5 μm).

Assembly	Alignment
SET9	Centred
SET10	$\frac{1}{4}$ Offset
SET12	Centred
SET13	Centred
SET15	Centred
SET16	$\frac{1}{2}$ Offset

Table 1.1.: A list of the detectors considered in this study, showing the misalignment of the HV-CMOS and CLICpix coupling pads.

1.3. Device Characterisation

The assemblies were characterised using a series of lab experiments as well as in realistic experimental conditions using the CERN SPS test beam. Due to the complexities of testing assemblies in a test beam, extensive lab test were performed first to characterise as many properties of the assemblies as possible. The lab experiments performed were as follows:

- **Radioactive source measurements**. The goal of this measurement is to examine both the output of the HV-CMOS voltage and the response of the CLICpix readout chip when a radioactive source is used to deposit charge within the HV-CMOS sensor.

- **Test pulse calibration of the CLICpix chip**. The goal of this measurement is to calibrate the response of the CLICpix sensor. This is achieved by injecting a voltage pulse of fixed height directly into the input of the chip and examining the output response.

1.3.1. Source Measurements

A radioactive source was used to deposit charge within the HV-CMOS sensor and used to characterise the response of the whole assembly. The HV-CMOS sensor converts the deposited charge into a voltage, which in turn passes through the capacitively coupled glue layer and into the CLICpix chip. Measurements were made of the output voltage produced by the HV-CMOS and the response of the CLICpix readout chip, in units of ToT. As the exact amount of charge deposited by the radioactive sources is unknown, this experiment focuses on examining the form of the voltage signal produced by the HV-CMOS and determining the response of the CLICpix chip as a function of this voltage. As the HV-CMOS signal must pass through the capacitively coupled glue layer before being measured by the CLICpix chip, this experiment characterises the behaviour of the gluing layer as well as the sensor and readout chips.

Experimental Setup

In order to characterise the samples, a Sr^{90} radioactive source was used to deposit charge in the HV-CMOS sensor. Sr^{90} undergoes β^- decay to form Y^{90}, which in turn undergoes β^- decay to form the stable isotope Z^{90}. Each β^- decay produces an e^- and a $\bar{\nu}_e$, with the e^- used to deposit charge in the HV-CMOS sensing layer. The Sr^{90} source used for this experiment had an activity of 29.6 MBq.

The radioactive source was positioned directly above the back-side of the HV-CMOS sensor, and measurements were made of both the ToT output from the CLICpix and the HV-CMOS analogue signal for individual pixels on the sensor. The HV-CMOS pulse shape was recorded on a fast sampling oscilloscope that was also used to trigger the CLICpix readout. The on-pixel event counter was used to veto events where multiple hits occurred within the active shutter period.

The HV-CMOS sensor was biased to 60 V during this experiment. The analogue output has a baseline voltage of $\approx$ 1.15 V, with signal saturation around a height of 700 mV. Examples of the HV-CMOS output can be seen in figure 1.5.
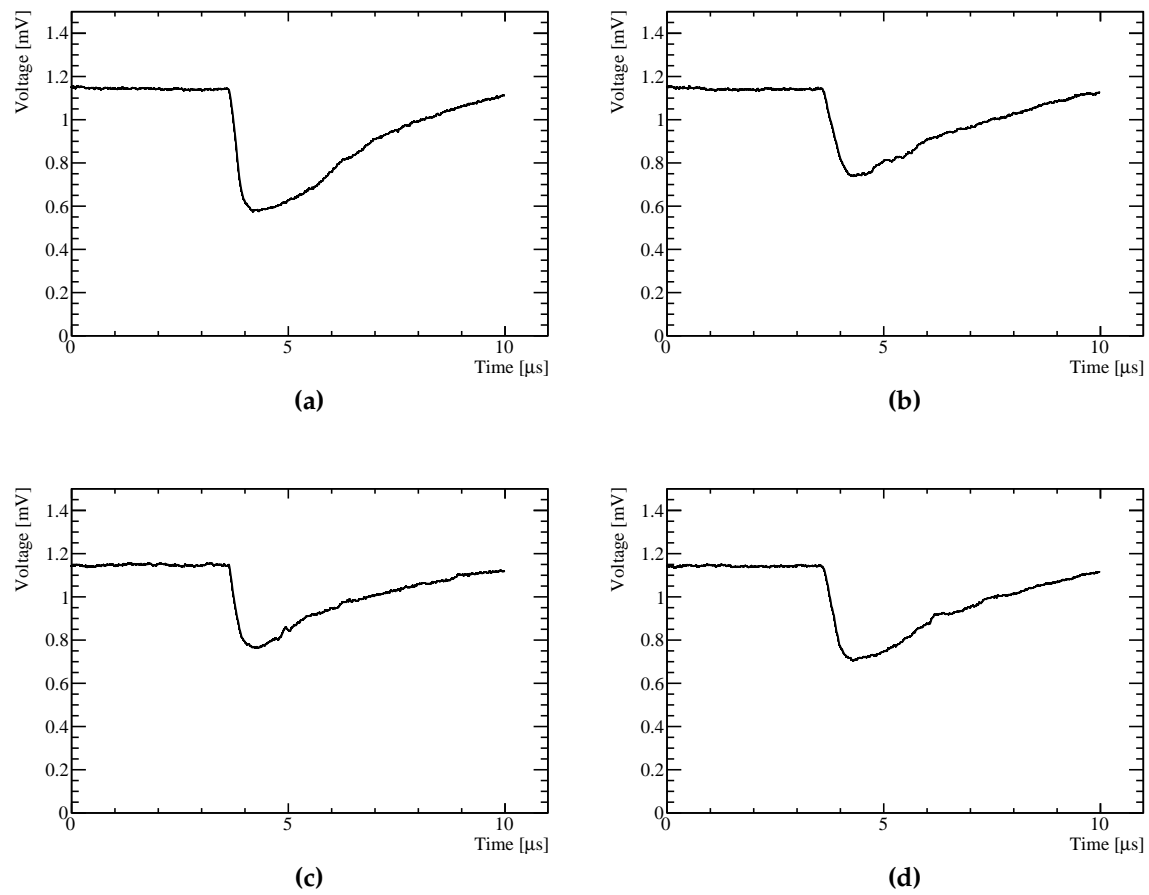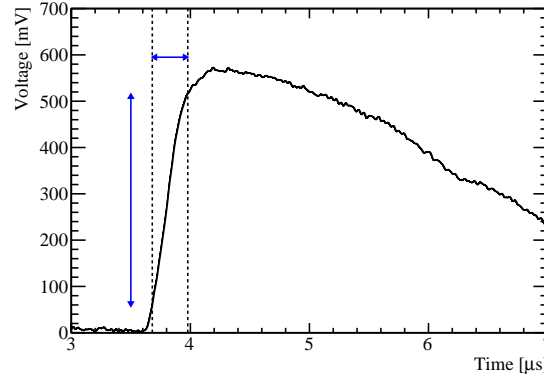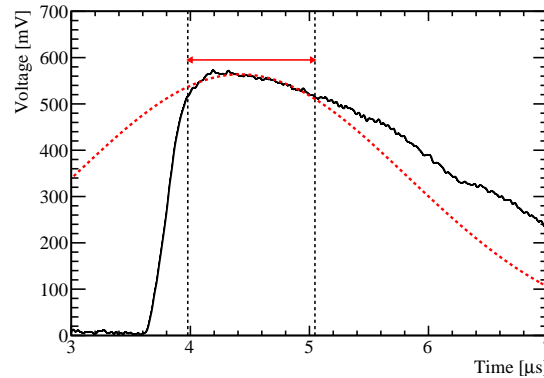
Figure 1.5.: HV-CMOS voltage pulses produced by radioactive Sr^{90} source.

(a) **Rise time determination.** The blue arrows show the change in time and voltage as the pulse goes from 10% to 90% of the raw pulse height. This time is used as the definition of the rise time in the subsequent analysis.

(b) **Pulse height determination.** The red dotted line is a Gaussian fit to the peak of the pulse. The peak is defined as the section of the signal above 90% of the raw pulse height.

Figure 1.6.: Analysis of HV-CMOS voltage as a function of time for pulses created by radioactive Sr^{90} source.

Analysis

The quantities of interest related to the HV-CMOS output are the pulse height and rise time. The baseline voltage was subtracted from the HV-CMOS analogue output and the pulse height inverted before the following analysis was applied.

The pulse height was taken as the mean of a Gaussian fit to the peak of the HV-CMOS output signal, defined as the section of the signal above 90% of the maximum recorded voltage change. The application of a Gaussian fit provides a more robust
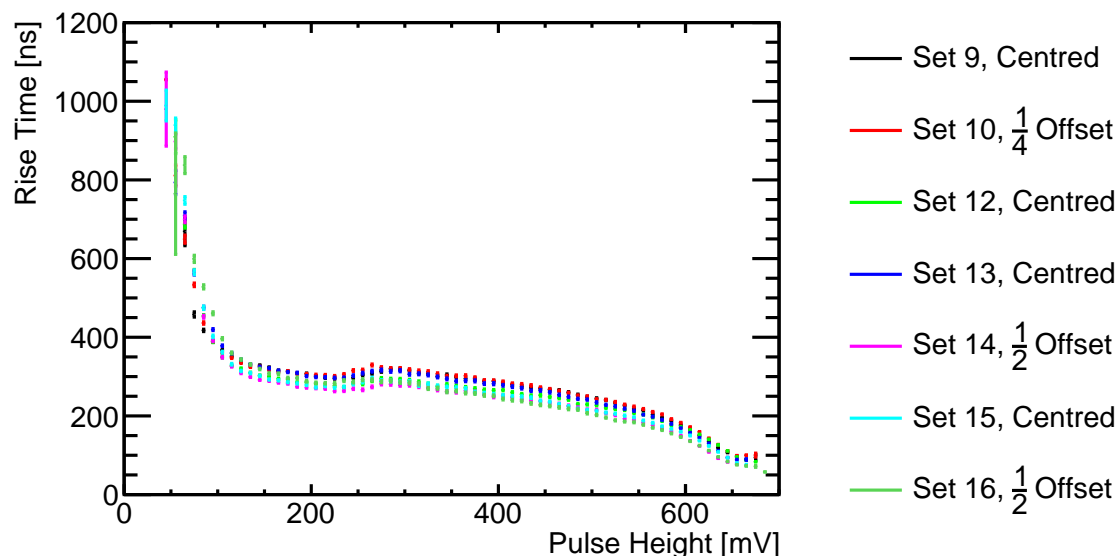
Figure 1.7.: HV-CMOS voltage rise time as a function of pulse height. CAN THE FRACTIONS BE MADE THE SAME SIZE AS THE REST OF THE TEXT?

metric for categorising the pulse height, which is less dependant on fluctuations in the voltage. The rise time was calculated as the time taken for the signal to go from 10% to 90% of the maximum recorded voltage change. This definition similarly makes the rise time metric more robust against fluctuations in the voltage. Examples of the calculation of these metrics for a representative pulse are shown in figure 1.6.

For each device the HV-CMOS pulse output was recorded for 15 pixels running along one edge of the 64 $\times$ 64 matrix; in the subsequent analysis the data for all 15 pixels is combined.

Results - Rise Time vs Pulse Height

The mean rise time as function of pulse height is shown in figure 1.7. This was determined by binning the events in terms of pulse height and determining the mean rise time for events in each of those bins. The pulse height was binned using a bin width of 4 mV ranging from 0 to 700 mV. At least 100 measurements per pulse height bin were used for the calculation of the average rise time. The error bars on this figure show the standard error in the mean rise time.
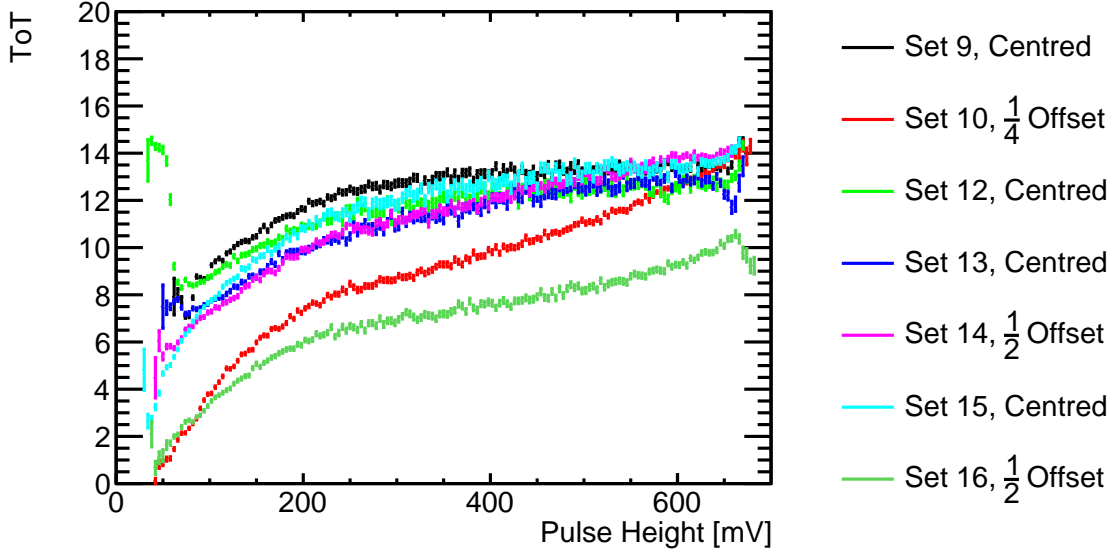
Figure 1.8.: CLICpix ToT as a function of HV-CMOS voltage pulse height. SAME COMMENT
TO LABELS AND FRACTION SIZES

The data in figure 1.7 shows that the rise time for the HV-CMOS front-end is approximately 300 ns across all samples, and that this is largely independent of pulse height for all but the smallest signals. For very small pulse heights (< 100 mV) rise times are significantly larger, suggesting that the deposited charge takes a longer time to be collected. This may be due to charge transport via diffusion rather than drift, giving a large increase in the time for the signal charge to be collected. At large values of deposited charge (higher output voltage), a gradual reduction in the rise time is observed, as expected for higher charge deposits. The similar characteristics for all samples makes the comparison of the different misaligned samples more straightforward, as the intrinsic HV-CMOS performance can be seen to be the same. The same must also be true of the CLICpix ASICS, which is indeed the case as the results in section **??** show.

Results - ToT vs Pulse Height

Figure 1.8 shows the mean ToT measured in the CLICpix as a function of the HV-CMOS output voltage pulse height. The determination of the mean and error bars for the ToT measurement is identical to that described in section 1.3.1 for the rise time measurement.

The distribution of mean ToT versus pulse height shows that for samples where the corresponding coupling pads are centred, the ToT increases with pulse height up to values of approximately 300 mV, and that the mean ToT saturates at ≈ 13. It is expected that the $\frac{1}{4}-$ and $\frac{1}{2}-$offset samples should have a lower ToT than the centred samples due to the lower effective capacitance between the HV-CMOS and CLICpix pads. The greater the offset is, the smaller the effective capacitance to the target CLICpix pad will be, and so the lower the recorded ToT. This is can be seen when comparing the centred samples to the $\frac{1}{4}-$offset sample and SET 16, the $\frac{1}{2}-$offset sample.

IN GENERAL YOU KEEP FORGETTING TO PUT THINGS IN CONTEXT - WHY CROSS-COUPLING?

Results - Cross Couplings

Due to the capacitive transfer of signal from the HV-CMOS sensor to the readout ASIC, it can be expected that any capacitance between the HV-CMOS pixel pads and the readout pads of neighbouring pixels may give rise to additional unwanted hits. Such cross-capacitancies can be observed in the same manner as the previous measurements, but by considering instead the ToT of the neighbouring CLICpix pixel. This is shown in figure 1.9a for all devices where the pixel pads are centred on each other, and in figure 1.9b for the $\frac{1}{4}-$offset sample and the $\frac{1}{2}-$offset sample, SET 16.

IN GENERAL USE "SET" INSTEAD OF "SET"

DO YOU HAVE A PLOT SHOWING THE NUMBER OF HITS IN THE NEIGH-BOUR? RELATIVE TO THE NUMBER OF HITS IN THE ALIGNED PIXEL? THIS PSEUDO-EFFICIENCY MIGHT BE A BETTER INDICATOR? FOLLOWED BY THESE PLOTS

SO: this part should be rewritten a little. Most likely you have a threshold effect at low pulse heights (not enough charge injected to make a hit, followed by enough to make a hit but just with a "default" low ToT). Then at high pulse heights you start to see a linear rise, which suggests you are now injecting enough charge to have a good correlation. But these are both second order to the point above, of showing that the number of hits in the main peak is N, and in the side peak is M « N (for low coupling).

REMOVE REFERENCES TO SET14!

No correlation between the adjacent pixel ToT and the HV-CMOS pulse height is observed for the samples shown in figure 1.9a for all but the lowest values of pulse height. The correlation observed at low pulse heights may arise due to the signal e⁻, which is primarily recorded in the target pixel, depositing a small amount of charge in the adjacent adjacent pixel. This can happen as the e⁻ may not be traveling normal to the pixel surface. However, as this feature is not present in all samples it could indicate a small misalignment exists in the samples showing the correlation.

There is, however, a strong correlation between adjacent pixel ToT and the HV-CMOS pulse height, shown in figure 1.9b, for SET 16, which is one of the $\frac{1}{2}$ offset samples. This distribution is almost identical to the the target pixel ToT distribution as a function of HV-CMOS pulse height, which is what would be expected given an equal signal charge sharing between the two readout ASICs. This indicates the charge sharing is well understood for this $\frac{1}{2}$ offset sample.

For the $\frac{1}{4}$ offset sample correlation is present only for low pulse heights as was the case for the centred samples. However, the mean ToT within the uncorrelated region is centred around ≈ 5 units of ToT, which is lower than was observed for the centred samples. This is due to the offset reducing the total capacitance between the HV-CMOS and CLICpix in comparison to the centred samples and thus reducing the ToT recorded.

Cross coupling was observed in one of the $\frac{1}{2}$ offset samples and, assuming that the other $\frac{1}{2}$ offset sample was manufactured incorrectly, then charge sharing was well understood for these $\frac{1}{2}$ offset samples. No cross coupling was observed for any of the other samples considered in this analysis.

THE RESULTS OF THIS SECTION SHOULD BE DISCUSSED AND I SHOULD TAKE A LOOK ONCE YOU HAVE CHANGED THE TEXT AROUND AGAIN.

1.3.2. Test Pulse Calibration

This measurement focuses upon determining the response of the CLICpix readout chip as a function of the input voltage entering the chip. The CLICpix readout chip allows for a fixed height voltage pulse to be directly applied at the input of the chip meaning a full calibration of the chip can be performed. This experiment extends the characterisation of the CLICpix chip beyond what was found using the radioactive
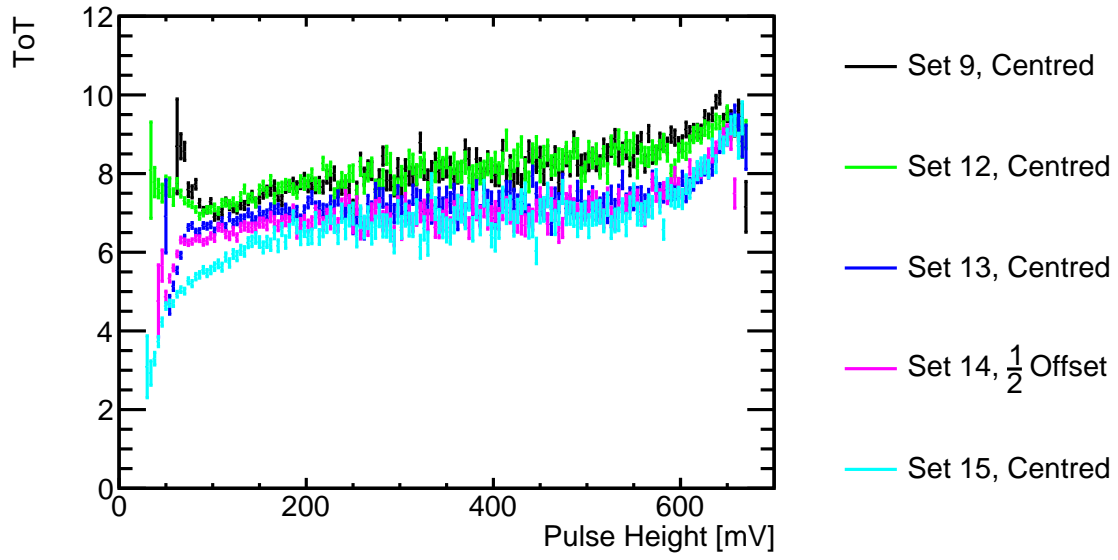
(a)
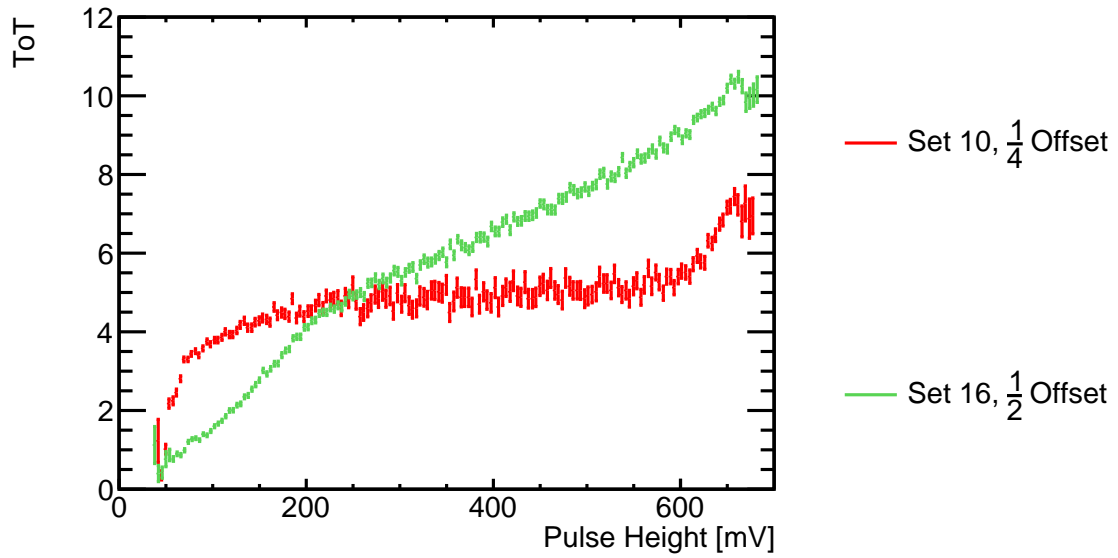
(b)

Figure 1.9.: CLICpix ToT on adjacent pixel along the direction of the offset as a function of HV-CMOS voltage pulse height.

source measurements as applying the voltage directly to the CLICpix fully isolates the response of the chip from effects relating to the glue layer.

I WOULD PRESENT A LITTLE MORE "STORY" STYLE, AND NOT SIMPLY AS A LIST OF UNRELATED EXPERIMENTS

In order to understand the charge transfer to the CLICpix, it is important to perform a calibration of the CLICpix front-end response. This was achieved by directly injecting a voltage pulse of fixed height directly into a capacitor held in each pixel, to inject a known quantity of charge. This gives a measure of the performance of the CLICpix independently of the HV-CMOS sensor.

Experimental Setup

In order to prevent any influence from neighbouring pixels during the testpulse measurements the matrix was pulsed in stages, with change injected into 1 out of every 16 pixels while masking the others. This was repeated 15 more times using different mask configurations until the entire matrix had been sampled. This procedure was repeated 100 times so that the average ToT on a per-pixel level could be recorded. The pulse height injected into the CLICpix varied from 2 to 180 mV in steps of 2 mV; an example of the mean ToT plotted against the injected pulse height is shown in figure 1.10.

Analysis

The functional form of the ToT against pulse height plot is described using a surrogate function as in [2], which is defined as

$$y = ax + b - \frac{c}{x - t} \tag{1.1}$$

where y is the ToT, x is the pulse height and a, b, c and t are fit parameters. For large pulse heights the linear relationship dominates while for low pulse heights the inversely proportional term dominates. c describes the curvature of the graph, while t determines the asymptote below which no signal is detected. Figure 1.11 shows an example of the application of this fit. As this function does not describe saturation of
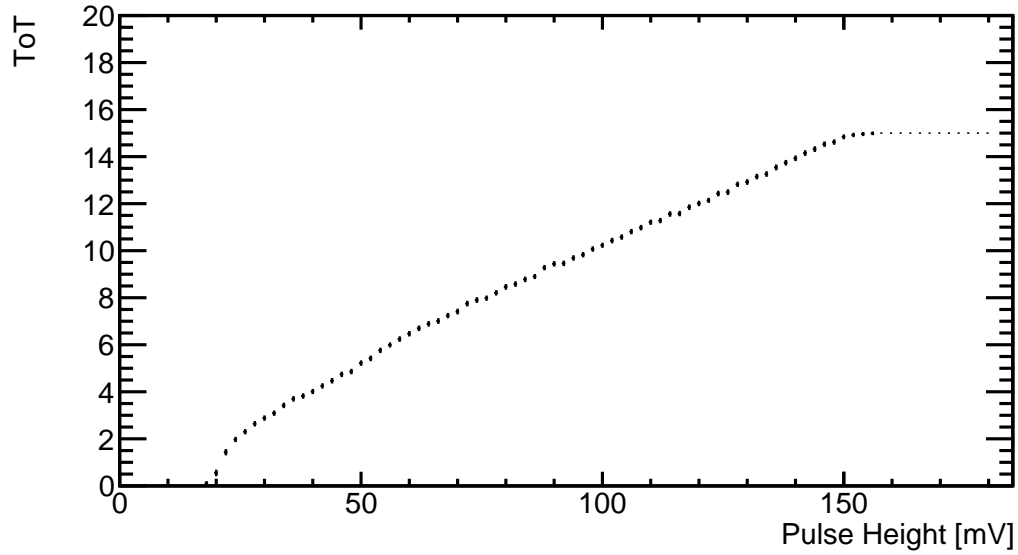
Figure 1.10.: CLICpix ToT as a function of injected pulse height for a single pixel. The black markers are the mean ToT and the error bars are the standard error on the mean.

Figure 1.11.: CLICpix ToT as a function of injected pulse height for a single pixel. The black markers are the mean ToT and the error bars are the standard error on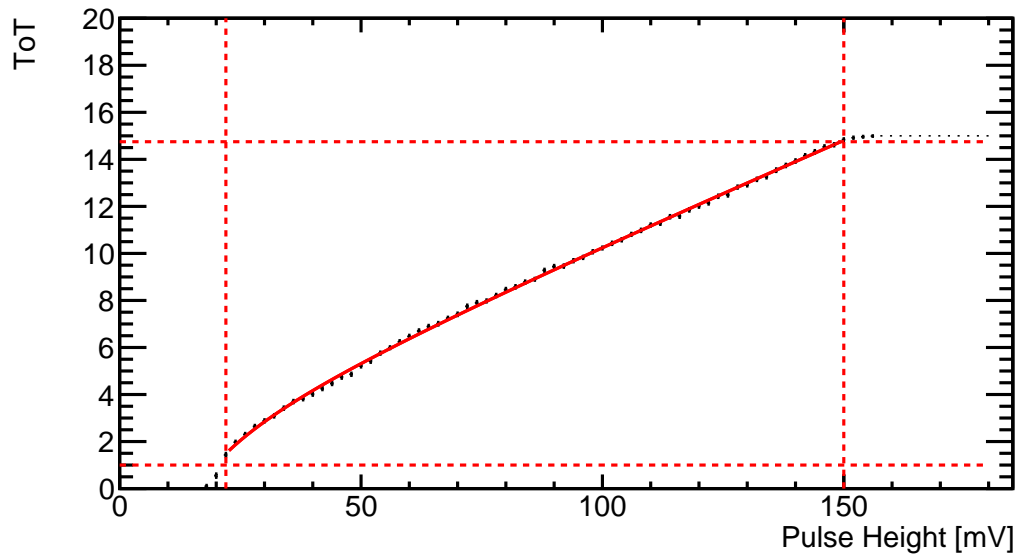 the mean. The solid red line shows the surrogate function fit and the dotted red lines show the range where the fit was applied.

the ToT or the region below threshold, the fit is only applied on data points where the mean ToT is greater than 1 and less than 14.75.

The application of this fit condenses the information for individual pixels to four parameters. These parameters can be averaged to categorise the CLICpix response across the matrix.

Results

A known issue withe the design of the CLICpix ASIC is an unwanted feedback capacitance between the discriminator output and amplifier input, leading to a fixed injected charge for each measured hit and operation of the chip at a higher-than-expected threshold. The magnitude of this effect is additionally different for odd and even columns due to the slightly differing physical layouts. This feature can be observed by examining the distribution of the fit parameters; these are shown for assembly SET9 in figure **??**. The peak at zero in the distribution of the a and b parameters, ≈ 150 in total, correspond to masked pixels in the detector. (CONFIRM THIS!) While the a and b parameters are centred around a single value, indicating a similar response in the linear region of the surrogate function, the c and t parameters are centred around one of two values. When examining the distribution of these parameters as a function of position on the matrix, shown in figure **??** for the same device, it can be seen that the structure is indeed related to the column a given pixel is in. This feature is present in all devices considered, and the underlying cause will be remedied in the next generation of the CLICpix ASIC.

I DONT KNOW WHAT THE FIRST PART OF THE CAPTION IS, BUT IF I HAVE CORRECTED THE SECOND PART (THAT APPEARS IN THE TEXT) PLEASE UPDATE THE FIRST PART IF IT IS RELEVANT AND SHOWN SOMEWHERE!

The matrix-averaged surrogate function fit parameters for all devices can be found in tables 1.2 and 1.3, for the even and odd columns respectively. The surrogate function using these average parameters as input is shown in figure 1.14.

REMOVE SET14

USE A TILDE TO SEPARATE NUMBER AND UNITS IN LATEX, THEN THE UNITS WILL NEVER BE PUT ONTO THE NEXT LINE

As figure 1.14 shows, the response of the CLICpix to the injected pulse height is rather uniform across all samples. In general, the turn-on pulse height is ≈ 10 mV and
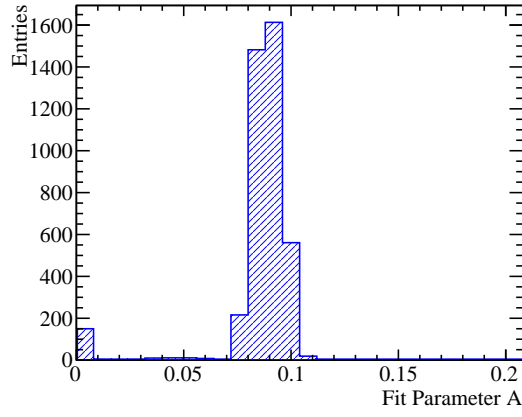
(a) *a* parameter.
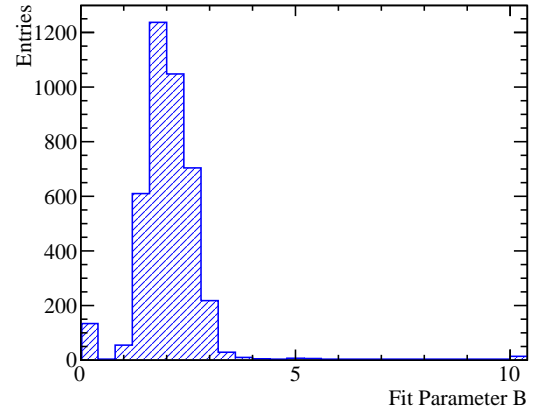
(b) *b* parameter.
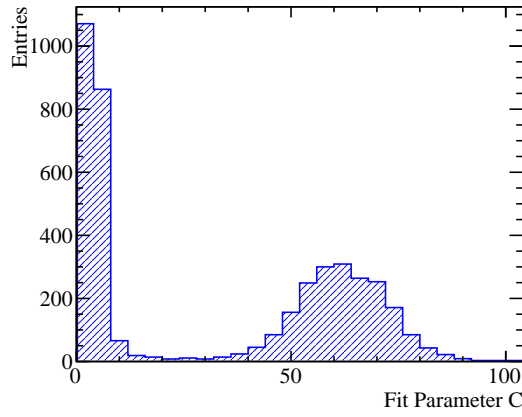
(c) *c* parameter.
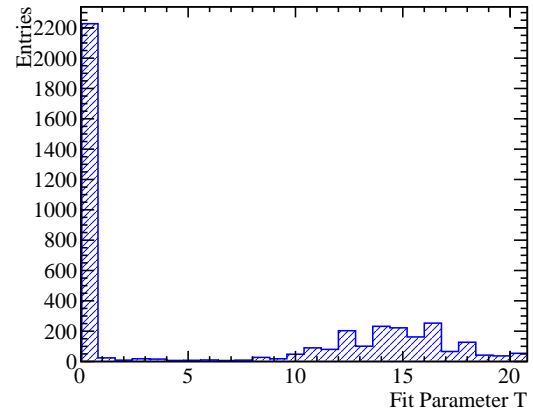
(d) *t* parameter.

Figure 1.12.: Distribution of surrogate function fit parameters for device SET 9.
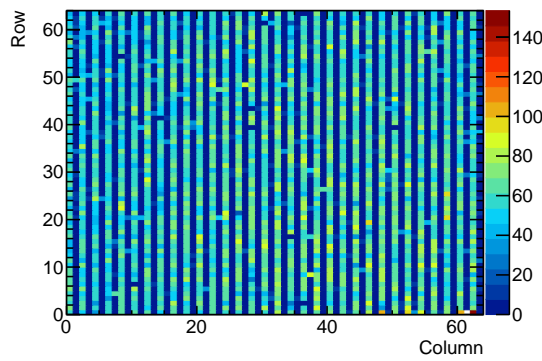
(a) *c* parameter.
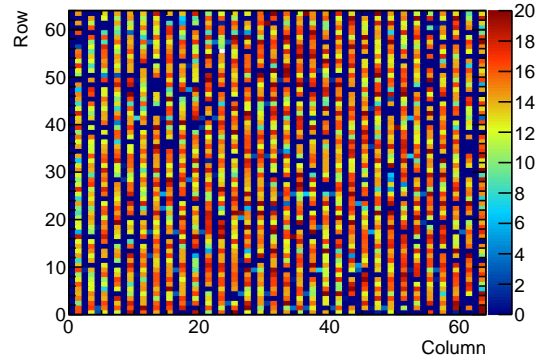
(b) *t* parameter.

Figure 1.13.: Distribution of surrogate function fit parameters *c* and *t* for device SET 9.

Assembly	a	b	c	t
SET 9	0.0875 ± 0.0005	2.41 ± 0.03	5.1 ± 0.1	12.79 ± 0.15
SET 10	0.0769 ± 0.0005	2.58 ± 0.03	7.5 ± 0.2	8.02 ± 0.14
SET 12	0.0725 ± 0.0005	2.87 ± 0.04	12.1 ± 0.3	7.86 ± 0.22
SET 13	0.0708 ± 0.0005	2.69 ± 0.03	16.2 ± 0.3	6.65 ± 0.18
SET 15	0.0856 ± 0.0005	2.34 ± 0.03	5.1 ± 0.2	12.51 ± 0.13
SET 16	0.0746 ± 0.0004	2.32 ± 0.02	13.7 ± 0.3	6.65 ± 0.16

Table 1.2.: Average fit parameters for even columns of the different CLICpix assemblies.

Assembly	a	b	c	t
SET 9	0.0834 ± 0.0003	1.72 ± 0.01	61.0 ± 0.3	0.25 ± 0.09
SET 10	0.0759 ± 0.0002	1.63 ± 0.01	43.2 ± 0.2	0.10 ± 0.02
SET 12	0.0731 ± 0.0003	1.92 ± 0.02	51.5 ± 0.3	0.36 ± 0.12
SET 13	0.0713 ± 0.0002	1.72 ± 0.01	52.5 ± 0.3	0.18 ± 0.07
SET 15	0.0836 ± 0.0003	1.52 ± 0.02	52.7 ± 0.3	0.42 ± 0.08
SET16	0.0727 ± 0.0002	1.49 ± 0.01	50.7 ± 0.2	0.10 ± 0.03

Table 1.3.: Average fit parameters for odd columns of the different CLICpix assemblies.

saturation (i.e. ToT of 15 units) occurs at ≈ 150 mV. For even-numbered columns there is a sharper rise in ToT than for odd-numbered columns due to the different quantity of (unwanted) injected charge. This effect was observed across all devices considered. The uniformity of the sample response ensures that differing effects between the assemblies produced with different misalignments are not due to the response of the CLICpix front end.

1.4. Test Beam Analysis

The lab based measurements have helped to describe many of the characteristics of the devices considered here, however, their use is limited as little information can be deduced about the incoming particles using lab based measurements. Therefore, to record device efficiencies it is necessary to place the device in a telescope to track the incoming and outgoing particles passing through the device. Furthermore, the radioactive source calibration cannot be used here as the particles produced by the
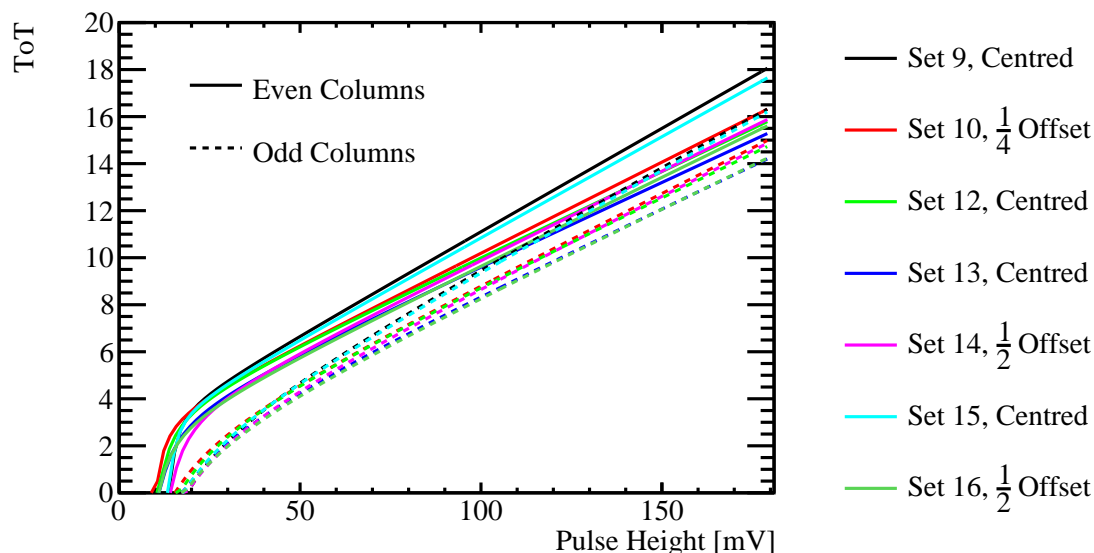
Figure 1.14.: Fitted ToT as a function of injected pulse height for all samples, averaged across the device matrix.

source would not be of high enough energy to pass through the entire telescope. This means that it is necessary to use a test beam in conjunction with the telescope to be able to full quantify the device characteristics.

AGAIN, BETTER INTRO? Describe a bit why we have to do testbeams, efficiency measurements, etc. Try not to present it in this detached "we have performed an experiment" - there is some reasoning behind this!

This sections describes the performance of the devices when placed under real experimental conditions at the CERN test beam area.

1.4.1. Test Beam Setup

COMBINED WITH ABOVE COMMENT The overall goal of this experiment was to determine the tracking performance of the capacitively coupled pixel sensors and to see whether the misalignment of the HV-CMOS and the CLICpix changes the performance. To that end the samples were mounted on a telescope and placed in a test beam to determine the efficiency, defined as the ratio of number of recorded tracks passing through device to the actual number of tracks passing through device, of the samples.

These test beam experiments were carried out in August and September 2015 on the H6 beam line in the CERN SPS North Area. The beam consisted of positively charged hadrons of momenta 120 GeV/c. Mean particle rates of 500 kHz/cm^2 were observed during the 4.8 s spills at intervals of 25 s. Is this data correct?.

AGAIN, MAYBE EXPAND THIS. You don't really explain why you need a telescope, or what it really is/is used for. Something like "in order to reconstruct the particle trajectory, several planes of detectors are used to..." etc.

During this experiment the samples mounted on an EUDET/AIDA telescope [6], which consists of six planes sensors using the Mimosa pixel technology. This telescope provides a resolution of 1.6 μm on the intercept position between tracks passing through the device and the device under test (DUT) mounted on it.

1.4.2. Analysis

The track position on the DUT is calculated using the measured particle trajectory through the telescope planes. This is followed by a search around the intercept position on the DUT to find an associated cluster; a region of 75 μm, or 3 pixels, about the intercept position is used. For multi-pixel clusters, the cluster position is calculated as the ToT-weighted centre-of-gravity. As tracks may undergo non-negligible multiple scattering, a χ^2 cut is used to remove less precisely reconstructed particles. Pixels identified on the DUT deemed to be noisy were removed from the analysis, along with any tracks intercepting within half a pixel. A pixel was deemed noisy if it responded at a mean rate greater than 5 σ in comparison to the average rate. Finally, all tracks occurring within 125 μm of each other were vetoed, in order to reduce the possibility of mis-association of clusters to tracks.

MAYBE SAY WHY ALIGNMENT IS NECESSARY? IN GENERAL THIS SECTION COULD DO WITH A LITTLE MORE CONTEXT

An alignment procedure was applied to both the telescope planes and the DUT, in order to account for the physical layout of the setup. The six telescope planes were aligned by producing rough tracks, and then varying the global alignment parameters of each plane in turn, in order to minimise the track χ^2. This was performed iteratively until no further gain was observed. After the telescope planes were aligned, the DUT
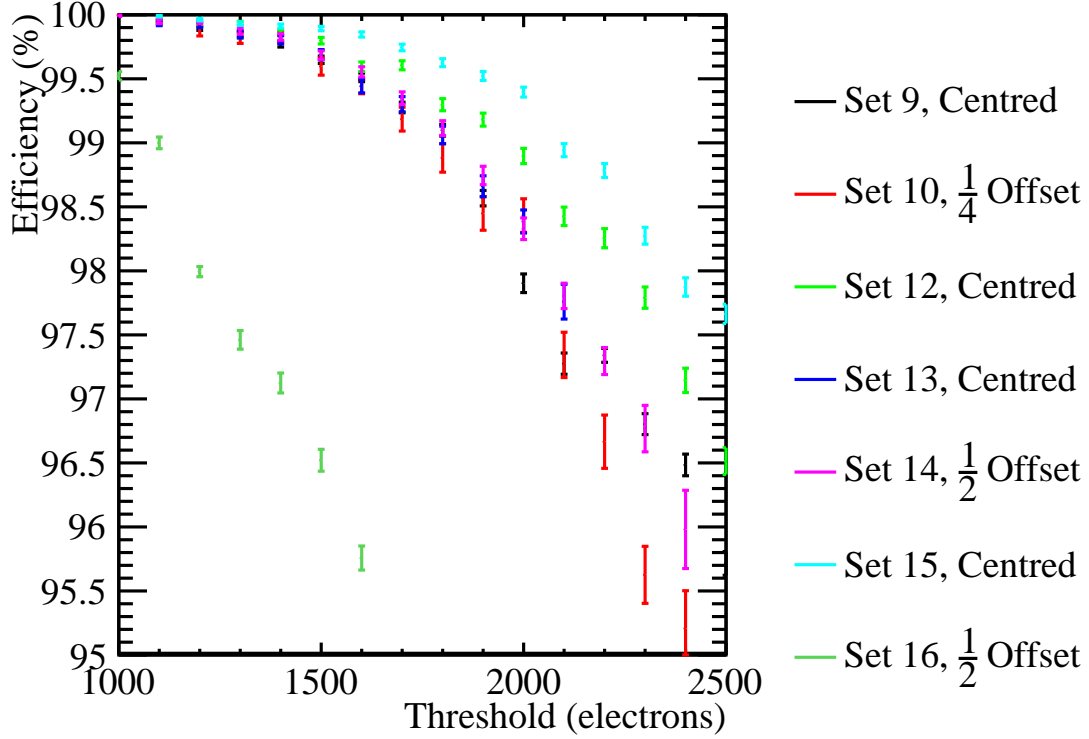
Figure 1.15.: Efficiency as a function of threshold.

was aligned by varying its alignment parameters in order to minimise the summed square of track residuals over many events.

AGAIN A BIT OF CONTEXT.

1.4.3. Single Hit Efficiency

The single hit efficiency, ϵ, is defined as the number of tracks with associated clusters in the CLICpix assembly, n, divided by the number of tracks reconstructed through the detector using the telescope, m. The errors shown on the efficiency measurements are given by $\sqrt{\frac{\epsilon(1-\epsilon)}{m}}$, which follows from the variance of n given binomial statistics with mean ϵ.

CONTEXT

CONTEXT (just in case you missed that ;-))

The efficiency as a function of threshold is shown in figure 1.15. The data indicates that, as expected, for all assemblies the single hit efficiency of the detector decreases when a higher amount of charge is required to generate a signal. However, it is clear that for the $\frac{1}{2}$ offset sample, SET 16, the efficiency is significantly lower in comparison to the other samples. There is a minor degradation in performance when considering the $\frac{1}{4}$ offset sample, but these results are still comparable to several of the centred samples. Overall, it can be concluded that manufacturing tolerances up to $\frac{1}{4}$ of a pixel width would not significantly affect performance.

AGAIN THIS NEEDS EXPANSION. You spent so much time on the earlier section, but now on the results you just say "see figure 1. end.". You can talk a bit more about the lower signal expected by reduced capacitance, etc.

1.5. Conclusions

Appendix A.

Pointless extras

"Le savant n'étudie pas la nature parce que cela est utile;
   il l'étudie parce qu'il y prend plaisir,
   et il y prend plaisir parce qu'elle est belle."
   — Henri Poincaré, 1854–1912

Appendixes (or should that be "appendices"?) make you look really clever, 'cos it's like you had more clever stuff to say than could be fitted into the main bit of your thesis. Yeah. So everyone should have at least three of them...

A.1. Anomalous Gauge Coupling Quartic Vertices Of Relevance in Vector Boson Scattering

The anomalous gauge couplings involving α_4 and α_5 arise in EFT through the addition of the following terms to the Lagrangian.

$$\text{Tr}(V^\mu V_\nu)]\text{Tr}(V^\nu V_\mu)] \text{ and } [\text{Tr}(V^\mu V_\mu)]^2 \tag{A.1}$$

Where V_μ is defined in the following way.

$$V_\mu = \Sigma (D_\mu \Sigma)^\dagger \tag{A.2}$$

and Σ, the Higgs field matrix, is defined as.

$$\Sigma = \exp(-\frac{i}{v}\mathbf{w}) \tag{A.3}$$

Where $\mathbf{w} = w^a \sigma^a$. w^a are the ... and σ^a are the Pauli spin matrices. The covariant derivative of the Higgs field matrix is

$$D_\mu \Sigma = (\partial_\mu + \frac{ig}{2}W_\mu - \frac{ig'}{2}B_\mu \sigma^3)\Sigma \tag{A.4}$$

For clarity consider the unitarity gauge where $\mathbf{w} = 0$, which implies $\Sigma = 1$. In this gauge V_μ takes the following form.

$$V_\mu = \frac{i}{2}(gW_\mu^i \sigma^i - g'B_\mu \sigma^3) = \frac{i}{2}\begin{pmatrix} gW_\mu^3 - g'B_\mu & g(W_\mu^1 - iW_\mu^2) \\ g(W_\mu^1 + iW_\mu^2) & -gW_\mu^3 + g'B_\mu \end{pmatrix}$$

$$= \frac{i}{2}\begin{pmatrix} \sqrt{g^2 + g'^2}Z_\mu & g\sqrt{2}W_\mu^+ \\ g\sqrt{2}W_\mu^- & \sqrt{g^2 + g'^2}Z_\mu \end{pmatrix}$$

Where the relationship between the mass and gauge symmetry basis are as follows.

$$W_\mu^+ = \frac{1}{\sqrt{2}}(W_\mu^1 - iW_\mu^2) \tag{A.5}$$

$$W_\mu^- = \frac{1}{\sqrt{2}}(W_\mu^1 + iW_\mu^2) \tag{A.6}$$

$$Z_\mu = c_w W_\mu^3 - s_w B_\mu \tag{A.7}$$

$$A_\mu = s_w W_\mu^3 + c_w B_\mu \tag{A.8}$$

With $c_w = \frac{g}{\sqrt{g^2+g'^2}}$ and $s_w = \frac{g'}{\sqrt{g^2+g'^2}}$. Consider the expansion of the terms to be incldued in the Lagrangian.

$$V^\mu V_\nu = \frac{-1}{4}\begin{pmatrix} \sqrt{g^2+g'^2}Z^\mu & g\sqrt{2}W^{+\mu} \\ g\sqrt{2}W^{-\mu} & \sqrt{g^2+g'^2}Z^\mu \end{pmatrix}\begin{pmatrix} \sqrt{g^2+g'^2}Z_\nu & g\sqrt{2}W_\nu^+ \\ g\sqrt{2}W_\nu^- & \sqrt{g^2+g'^2}Z_\nu \end{pmatrix} \quad (A.9)$$

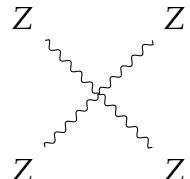$$\mathrm{Tr}[V^\mu V_\nu] = \frac{-1}{2}((g^2+g'^2)Z^\mu Z_\nu + g^2 W^{+\mu}W_\nu^- + g^2 W^{-\mu}W_\nu^+) \quad (A.10)$$

$$\mathrm{Tr}[V^\mu V_\nu]\mathrm{Tr}[V_\mu V^\nu] = \frac{(g^2+g'^2)^2}{4}(Z^\mu Z_\mu)^2 + g^2(g^2+g'^2)(Z^\mu Z^\nu W_\mu^- W_\nu^+) \quad (A.11)$$

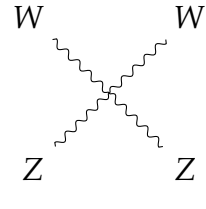$$+\frac{g^4}{2}(W^{-\mu}W_\mu^+)^2 + \frac{g^4}{2}(W^{-\mu}W^{+\nu}W_\mu^- W_\nu^+) \quad (A.12)$$

$$\mathrm{Tr}[V^\mu V_\mu]^2 = \frac{(g^2+g'^2)^2}{4}(Z^\mu Z_\mu)^2 + g^2(g^2+g'^2)(Z^\mu Z^\nu W_\mu^- W_\nu^+) \quad (A.13)$$

$$+g^4(W^{-\mu}W_\mu^+)^2 \quad (A.14)$$
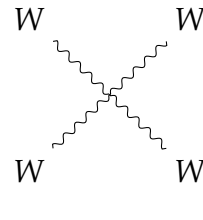
These two terms change the cross section for the vector boson scattering processes at CLIC that involve $ZZ \to ZZ$, $W^+W^- \to ZZ$, $ZZ \to W^+W^-$ and $W^+W^- \to W^+W^-$.

$$\subset (\alpha_4 + \alpha_5)\frac{(g^2+g'^2)^2}{4} \quad (A.15)$$

$$W \quad W$$
$$Z \quad Z \quad \subset (\alpha_4 + \alpha_5)g^2(g^2 + g'^2) \tag{A.16}$$

$$W \quad W$$
$$W \quad W \quad \subset (\alpha_4 + 2\alpha_5)\frac{g^4}{2} \text{ and } \frac{g^4}{2}\alpha_4 \tag{A.17}$$

A.2. χ^2 Contour Plots for Jet Algorithm Optimisation

(a) Longitudinally Invariant Kt Algorithm, R = 0.7, Loose Selected PFOs, 1.4 TeV Events

(b) Longitudinally Invariant Kt Algorithm, R = 0.9, Loose Selected PFOs, 1.4 TeV Events

(c) Longitudinally Invariant Kt Algorithm, R = 1.1, Loose Selected PFOs, 1.4 TeV Events

(d) Longitudinally Invariant Kt Algorithm, R = 0.7, Selected PFOs, 1.4 TeV Events

(e) Longitudinally Invariant Kt Algorithm, R = 0.9, Selected PFOs, 1.4 TeV Events

(f) Longitudinally Invariant Kt Algorithm, R = 1.1, Selected PFOs, 1.4 TeV Events

(g) Longitudinally Invariant Kt Algorithm, R = 0.7, Tight Selected PFOs, 1.4 TeV Events

(h) Longitudinally Invariant Kt Algorithm, R = 0.9, Tight Selected PFOs, 1.4 TeV Events

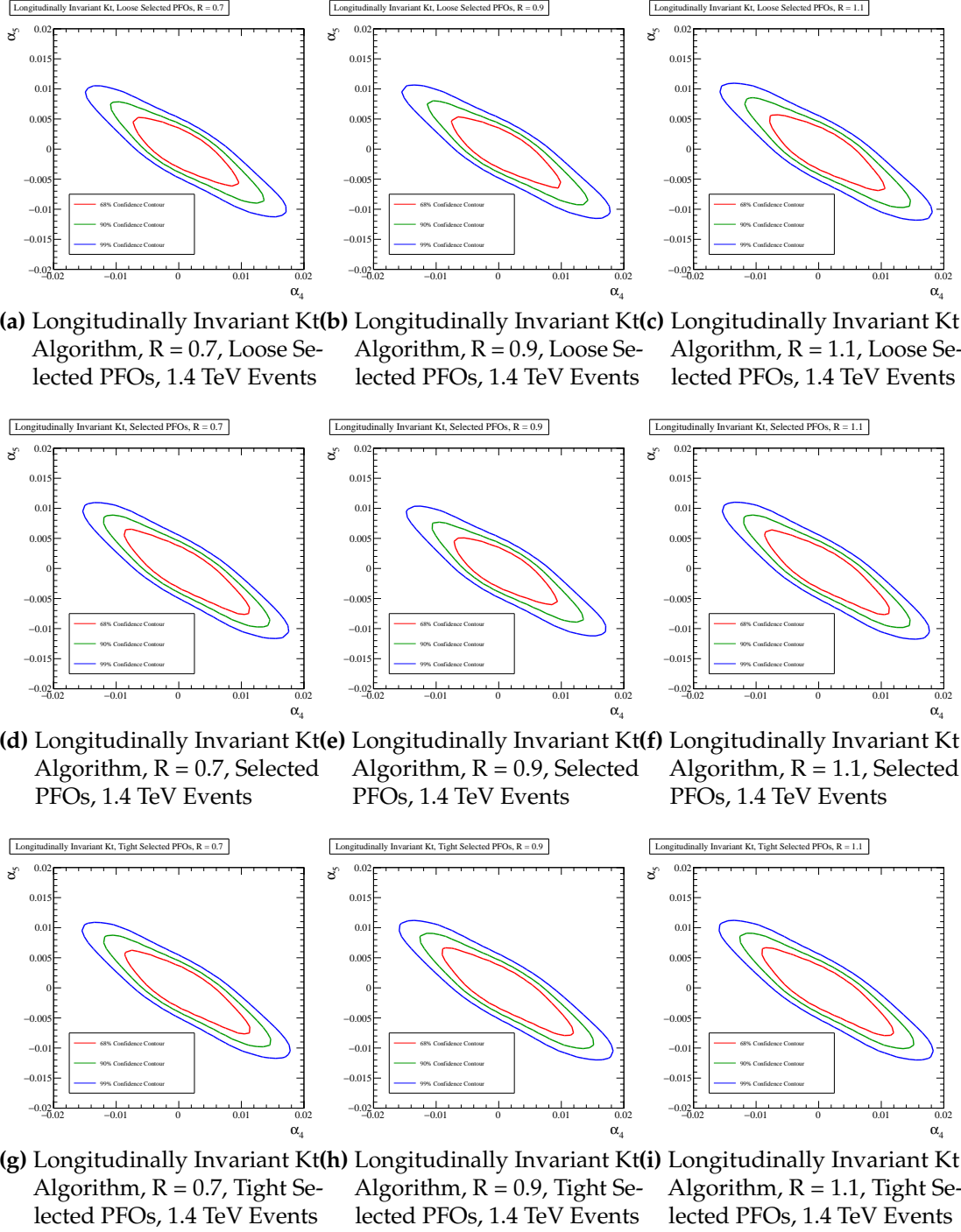**(i)** Longitudinally Invariant Kt Algorithm, R = 1.1, Tight Selected PFOs, 1.4 TeV Events

Figure A.1.: χ^2 Sensitivity contours for the qqqq$\nu\nu$ final state arising from a fit to $\cos\theta^*_{\text{Jets}}$ at 1.4 TeV for different values of jet reconstruction parameters.
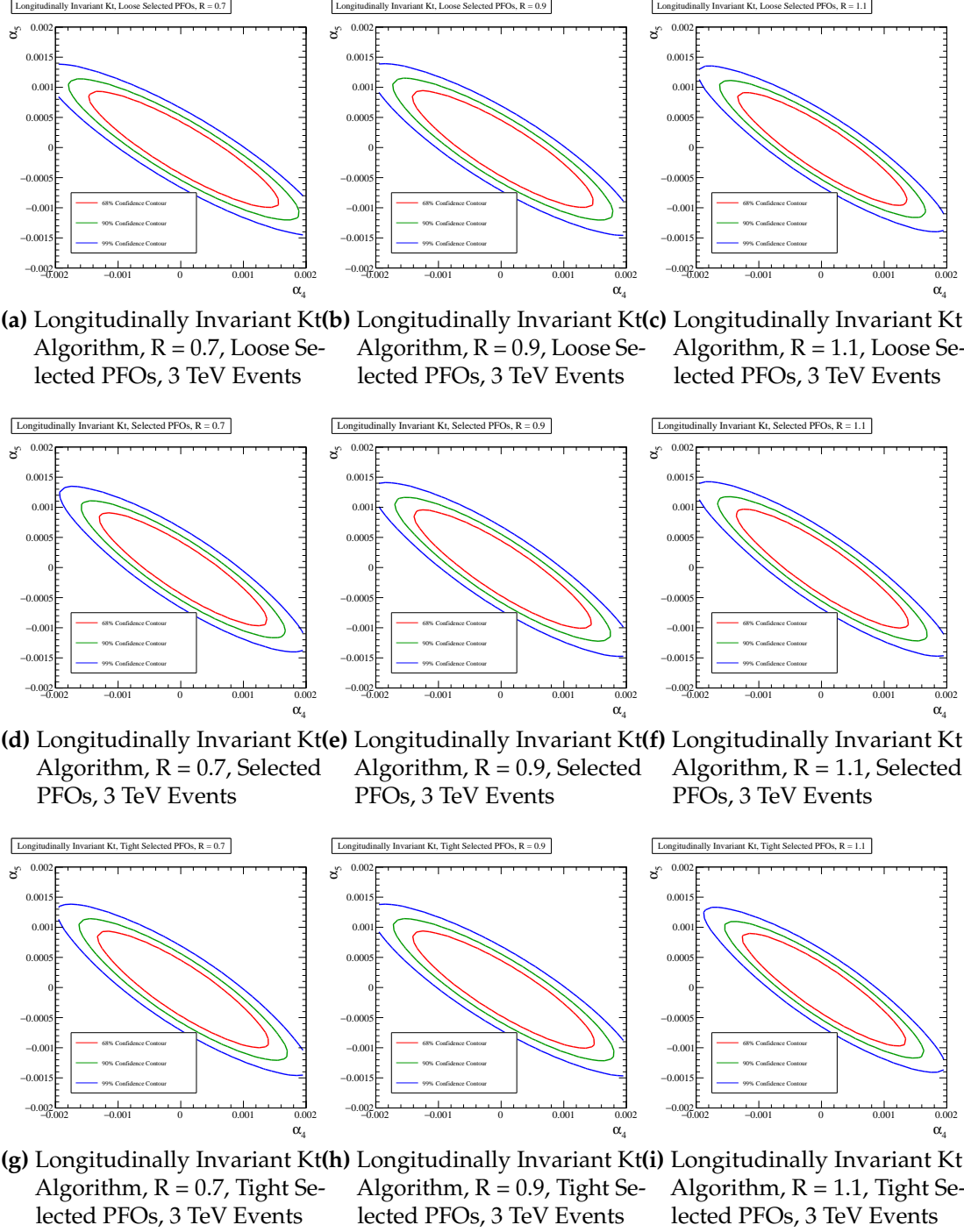
(a) Longitudinally Invariant Kt Algorithm, R = 0.7, Loose Selected PFOs, 3 TeV Events

(b) Longitudinally Invariant Kt Algorithm, R = 0.9, Loose Selected PFOs, 3 TeV Events

(c) Longitudinally Invariant Kt Algorithm, R = 1.1, Loose Selected PFOs, 3 TeV Events

(d) Longitudinally Invariant Kt Algorithm, R = 0.7, Selected PFOs, 3 TeV Events

(e) Longitudinally Invariant Kt Algorithm, R = 0.9, Selected PFOs, 3 TeV Events

(f) Longitudinally Invariant Kt Algorithm, R = 1.1, Selected PFOs, 3 TeV Events

(g) Longitudinally Invariant Kt Algorithm, R = 0.7, Tight Selected PFOs, 3 TeV Events

(h) Longitudinally Invariant Kt Algorithm, R = 0.9, Tight Selected PFOs, 3 TeV Events

(i) Longitudinally Invariant Kt Algorithm, R = 1.1, Tight Selected PFOs, 3 TeV Events

Figure A.2.: χ^2 Sensitivity contours for the $qqqq\nu\nu$ final state arising from a fit to $\cos\theta^*_{\text{Jets}}$ at 1.4 TeV for different values of jet reconstruction parameters.

Colophon

This thesis was made in LaTeX 2_ε using the "hepthesis" class [4].

Bibliography

[1] Roel Aaij, Bernardo Adeva, Marco Adinolfi, Ziad Ajaltouni, Simon Akar, Johannes Albrecht, Federico Alessio, Michael Alexander, Suvayu Ali, Georgy Alkhazov, Paula Alvarez Cartelle, Antonio Augusto Alves Jr, Sandra Amato, Silvia Amerio, Yasmine Amhis, Liupan An, Lucio Anderlini, Guido Andreassi, Mirco Andreotti, Jason Andrews, Mario Anelli, Robert Appleby, Flavio Archilli, Philippe d'Argent, Joan Arnau Romeu, Alexander Artamonov, Marina Artuso, Elie Aslanides, Giulio Auriemma, Marouen Baalouch, Igor Babuschkin, Sebastian Bachmann, John Back, Alexey Badalov, Clarissa Baesso, Sophie Baker, Vladislav Balagura, Wander Baldini, Alessandro Balla, Alexander Baranov, Roger Barlow, Colin Barschel, Sergey Barsuk, William Barter, Fedor Baryshnikov, Mateusz Baszczyk, Varvara Batozskaya, Baasansuren Batsukh, Vincenzo Battista, Aurelio Bay, Leo Beaucourt, John Beddow, Franco Bedeschi, Ignacio Bediaga, Andrew Beiter, Lennaert Bel, Violaine Bellee, Nicoletta Belloli, Konstantin Belous, Ivan Belyaev, Eli Ben-Haim, Giovanni Bencivenni, Sean Benson, Sarah Beranek, Alexander Berezhnoy, Roland Bernet, Alessandro Bertolin, Christopher Betancourt, Federico Betti, Marc-Olivier Bettler, Martinus van Beuzekom, Iaroslava Bezshyiko, Simone Bifani, Pierre Billoir, Alex Birnkraut, Alexander Bitadze, Andrea Bizzeti, Thomas Blake, Frederic Blanc, Johan Blouw, Steven Blusk, Valerio Bocci, Thomas Boettcher, Alexander Bondar, Nikolay Bondar, Walter Bonivento, Igor Bordyuzhin, Alessio Borgheresi, Silvia Borghi, Maxim Borisyak, Martino Borsato, Francesco Bossu, Meriem Boubdir, Themistocles Bowcock, Espen Eie Bowen, Concezio Bozzi, Svende Braun, Thomas Britton, Jolanta Brodzicka, Davide Brundu, Emma Buchanan, Christopher Burr, Albert Bursche, Jan Buytaert, Sandro Cadeddu, Roberto Calabrese, Marta Calvi, Miriam Calvo Gomez, Alessandro Camboni, Pierluigi Campana, Daniel Hugo Campora Perez, Lorenzo Capriotti, Angelo Carbone, Giovanni Carboni, Roberta Cardinale, Alessandro Cardini, Maurizio Carletti, Paolo Carniti, Laurence Carson, Kazuyoshi Carvalho Akiba, Gianluigi Casse, Lorenzo Cassina, Lucia Castillo Garcia, Luigi Casu, Marco Cattaneo, Giovanni Cavallero, Riccardo Cenci, David

Chamont, Matthew Charles, Philippe Charpentier, Georgios Chatzikonstantinidis, Maximilien Chefdeville, Shanzhen Chen, Shu-Faye Cheung, Veronika Chobanova, Marcin Chrzaszcz, Alexsei Chubykin, Paolo Ciambrone, Xabier Cid Vidal, Gregory Ciezarek, Mauro Citterio, Peter Clarke, Marco Clemencic, Harry Cliff, Joel Closier, Victor Coco, Simone Coelli, Julien Cogan, Eric Cogneras, Violetta Cogoni, Lucian Cojocariu, Paula Collins, Albert Comerma-Montells, Andrea Contu, Andrew Cook, George Coombs, Samuel Coquereau, Gloria Corti, Marco Corvo, Cayo Mar Costa Sobral, Benjamin Couturier, Greig Cowan, Daniel Charles Craik, Andrew Crocombe, Melissa Maria Cruz Torres, Samuel Cunliffe, Robert Currie, Carmelo D'Ambrosio, Franciole Da Cunha Marinho, Elena Dall'Occo, Jeremy Dalseno, Pieter David, Adam Davis, Kristof De Bruyn, Stefano De Capua, Michel De Cian, Jussara De Miranda, Leandro De Paula, Marilisa De Serio, Patrizia De Simone, Cameron Thomas Dean, Daniel Decamp, Mirko Deckenhoff, Luigi Del Buono, Moritz Demmer, Adam Dendek, Denis Derkach, Olivier Deschamps, Francesco Dettori, Biplab Dey, Angelo Di Canto, Pasquale Di Nezza, Hans Dijkstra, Francesca Dordei, Mirco Dorigo, Alvaro Dosil SuÃąrez, Anatoliy Dovbnya, Karlis Dreimanis, Laurent Dufour, Giulio Dujany, Kevin Dungs, Paolo Durante, Rustem Dzhelyadin, Agnieszka Dziurda, Alexey Dzyuba, Nicolas DÃľlÃľage, Sajan Easo, Marcus Ebert, Ulrik Egede, Victor Egorychev, Semen Eidelman, Stephan Eisenhardt, Ulrich Eitschberger, Robert Ekelhof, Lars Eklund, Scott Ely, Sevda Esen, Hannah Mary Evans, Timothy Evans, Antonio Falabella, Nathanael Farley, Stephen Farry, Robert Fay, Davide Fazzini, Giulietto Felici, Dianne Ferguson, Gerard Fernandez, Antonio Fernandez Prieto, Fabio Ferrari, Fernando Ferreira Rodrigues, Massimiliano Ferro-Luzzi, Sergey Filippov, Rosa Anna Fini, Marco Fiore, Massimiliano Fiorini, Miroslaw Firlej, Conor Fitzpatrick, Tomasz Fiutowski, Frederic Fleuret, Klaus Fohl, Marianna Fontana, Flavio Fontanelli, Dean Charles Forshaw, Roger Forty, Vinicius Franco Lima, Markus Frank, Christoph Frei, Paolo Fresch, Jinlin Fu, Wolfgang Funk, Emiliano Furfaro, Christian FÃd'rber, Abraham Gallas Torreira, Domenico Galli, Stefano Gallorini, Silvia Gambetta, Miriam Gandelman, Paolo Gandini, Yuanning Gao, Luis Miguel Garcia Martin, JuliÃąn GarcÃ■a PardiÃśas, Jordi Garra Tico, Lluis Garrido, Philip John Garsed, David Gascon, Clara Gaspar, Maurizio Gatta, Laura Gavardi, Giulio Gazzoni, David Gerick, Evelina Gersabeck, Marco Gersabeck, Timothy Gershon, Philippe Ghez, Sebastiana GianÃň, Valerie Gibson, Olivier GÃűran Girard, Lavinia-Helena Giubega, Konstantin Gizdov, Vladimir Gligorov, Dmitry Golubkov, Andrey Golutvin, Alvaro Gomes, Igor Vladimirovich Gorelov, Claudio Gotti, Ekaterina Govorkova, Ricardo Gra-

ciani Diaz, Luis Alberto Granado Cardoso, Eugeni GraugÃľs, Elena Graverini, Giacomo Graziani, Alexandru Grecu, Roman Greim, Peter Griffith, Lucia Grillo, Barak Raimond Gruberg Cazon, Oliver GrÃijnberg, Evgeny Gushchin, Yury Guz, Thierry Gys, Carla GÃűbel, Thomas Hadavizadeh, Christos Hadjivasiliou, Guido Haefeli, Christophe Haen, Susan Haines, Brian Hamilton, Xiaoxue Han, Stephanie Hansmann-Menzemer, Neville Harnew, Samuel Harnew, Jonathan Harrison, Mark Hatch, Jibo He, Timothy Head, Arno Heister, Karol Hennessy, Pierre Henrard, Louis Henry, Eric van Herwijnen, Miriam HeÃ§, AdlÃĺne Hicheur, Donal Hill, Christoph Hombach, P H Hopchev, Zachary Huard, Wouter Hulsbergen, Thibaud Humair, Mikhail Hushchyn, David Hutchcroft, Marek Idzik, Philip Ilten, Richard Jacobsson, Pawel Jalocha, Eddy Jans, Abolhassan Jawahery, Feng Jiang, Malcolm John, Daniel Johnson, Christopher Jones, Christian Joram, Beat Jost, Nathan Jurik, Sergii Kandybei, Matthias Karacson, James Mwangi Kariuki, Sarah Karodia, Matthieu Kecke, Matthew Kelsey, Matthew Kenzie, Tjeerd Ketel, Egor Khairullin, Basem Khanji, Chitsanu Khurewathanakul, Thomas Kirn, Suzanne Klaver, Konrad Klimaszewski, Tatsiana Klimkovich, Serhii Koliiev, Michael Kolpin, Ilya Komarov, Patrick Koppenburg, Alena Kosmyntseva, Sofia Kotriakhova, Anastasiia Kozachuk, Mohamad Kozeiha, Leonid Kravchuk, Katharina Kreplin, Michal Kreps, Pavel Krokovny, Florian Kruse, Wojciech Krzemien, Wojciech Kucewicz, Marcin Kucharczyk, Vasily Kudryavtsev, Axel Kevin Kuonen, Krzysztof Kurek, Tengiz Kvaratskheliya, Daniel Lacarrere, George Lafferty, Adriano Lai, Christoph Langenbruch, Thomas Latham, Cristina Lazzeroni, Renaud Le Gac, Jeroen van Leerdam, Alexander Leflat, Jacques LefranÃğois, Regis LefÃĺvre, Florian Lemaitre, Edgar Lemos Cid, Olivier Leroy, Tadeusz Lesiak, Blake Leverington, Tenglin Li, Yiming Li, Zhuoming Li, Tatiana Likhomanenko, Rolf Lindner, Federica Lionetto, Xuesong Liu, David Loh, Angelo Loi, Iain Longstaff, Jose Lopes, Donatella Lucchesi, Miriam Lucio Martinez, Haofei Luo, Anna Lupato, Eleonora Luppi, Oliver Lupton, Alberto Lusiani, Xiao-Rui Lyu, Frederic Machefert, Florin Maciuc, Oleg Maev, Kevin Maguire, Sneha Malde, Alexander Malinin, Timofei Maltsev, Giulia Manca, Giampiero Mancinelli, Peter Michael Manning, Jan Maratas, Jean FranÃğois Marchand, Umberto Marconi, Carla Marin Benito, Matthieu Marinangeli, Pietro Marino, JÃűrg Marks, Davide Marras, Giuseppe Martellotti, Morgan Martin, Maurizio Martinelli, Diego Martinez Santos, Fernando Martinez Vidal, Danielle Martins Tostes, Laure Marie Massacrier, AndrÃľ Massafferri, Rosen Matev, Abhijit Mathad, Zoltan Mathe, Clara Matteuzzi, Andrea Mauri, Emilie Maurice, Brice Maurin, Alexander Mazurov, Michael McCann, Andrew McNab, Ronan McNulty, Brian Meadows,

Frank Meier, Dmytro Melnychuk, Marcel Merk, Andrea Merli, Emanuele Michielin, Diego Alejandro Milanes, Marie-Noelle Minard, Dominik Stefan Mitzel, Andrea Mogini, Josue Molina Rodriguez, Igancio Alberto Monroy, Stephane Monteil, Mauro Morandin, Piotr Morawski, Michael Joseph Morello, Olga Morgunova, Jakub Moron, Adam Benjamin Morris, Raymond Mountain, Franz Muheim, Mick Mulder, Manuel Mussini, Dominik MÃijller, Janine MÃijller, Katharina MÃijller, Vanessa MÃijller, Paras Naik, Tatsuya Nakada, Raja Nandakumar, Anita Nandi, Irina Nasteva, Matthew Needham, Nicola Neri, Sebastian Neubert, Niko Neufeld, Max Neuner, Thi Dung Nguyen, Chung Nguyen-Mau, Simon Nieswand, Ramon Niet, Nikolay Nikitin, Thomas Nikodem, Alla Nogay, Alexey Novoselov, Daniel Patrick O'Hanlon, Agnieszka Oblakowska-Mucha, Vladimir Obraztsov, Stephen Ogilvy, Rudolf Oldeman, Gerco Onderwater, Juan Martin Otalora Goicochea, Adam Otto, Patrick Owen, Maria Aranzazu Oyanguren, Preema Rennee Pais, Antimo Palano, Matteo Palutan, Antonios Papanestis, Marco Pappagallo, Luciano Pappalardo, Cheryl Pappenheimer, William Parker, Christopher Parkes, Giovanni Passaleva, Alessandra Pastore, Mitesh Patel, Claudia Patrignani, Alex Pearce, Antonio Pellegrino, Gianni Penso, Monica Pepe Altarelli, Stefano Perazzini, Pascal Perret, Luca Pescatore, Konstantinos Petridis, Alessandro Petrolini, Aleksandr Petrov, Marco Petruzzo, Eduardo Picatoste Olloqui, Boleslaw Pietrzyk, Malgorzata Pikies, Davide Pinci, Alessandro Pistone, Alessio Piucci, Vlad-Mihai Placinta, Stephen Playfer, Maximo Plo Casasus, Tuomas Poikela, Francesco Polci, Marco Poli Lener, Anton Poluektov, Ivan Polyakov, Erica Polycarpo, Gabriela Johanna Pomery, Sebastien Ponce, Alexander Popov, Dmitry Popov, Bogdan Popovici, Stanislav Poslavskii, CÃl'dric Potterat, Eugenia Price, Jessica Prisciandaro, Claire Prouve, Valery Pugatch, Albert Puig Navarro, Giovanni Punzi, Chen Qian, Wenbin Qian, Renato Quagliani, Bartolomiej Rachwal, Jonas Rademacker, Matteo Rama, Miguel Ramos Pernas, Murilo Rangel, Iurii Raniuk, Fedor Ratnikov, Gerhard Raven, Federico Redi, Stefanie Reichert, Alberto dos Reis, Clara Remon Alepuz, Victor Renaudin, Stefania Ricciardi, Sophie Richards, Mariana Rihl, Kurt Rinnert, Vicente Rives Molina, Patrick Robbe, Ana Barbara Rodrigues, Eduardo Rodrigues, Jairo Alexis Rodriguez Lopez, Pablo Rodriguez Perez, Alexey Rogozhnikov, Stefan Roiser, Alexandra Paige Rollings, Vladimir Romanovskiy, Antonio Romero Vidal, John William Ronayne, Marcello Rotondo, Matthew Scott Rudolph, Thomas Ruf, Pablo Ruiz Valls, Juan Jose Saborido Silva, Elnur Sadykhov, Naylya Sagidova, Biagio Saitta, Valdir Salustino Guimaraes, David Sanchez Gonzalo, Carlos Sanchez Mayordomo, Brais Sanmartin Sedes, Roberta Santacesaria, Cibran Santa-

marina Rios, Marco Santimaria, Emanuele Santovetti, Alessandro Saputi, Alessio Sarti, Celestina Satriano, Alessia Satta, Daniel Martin Saunders, Darya Savrina, Stefan Schael, Margarete Schellenberg, Manuel Schiller, Heinrich Schindler, Maximilian Schlupp, Michael Schmelling, Timon Schmelzer, Burkhard Schmidt, Olivier Schneider, Andreas Schopper, HF Schreiner, Konstantin Schubert, Maxime Schubiger, Marie Helene Schune, Rainer Schwemmer, Barbara Sciascia, Adalberto Sciubba, Alexander Semennikov, Antonino Sergi, Nicola Serra, Justine Serrano, Lorenzo Sestini, Paul Seyfert, Mikhail Shapkin, Illya Shapoval, Yury Shcheglov, Tara Shears, Lev Shekhtman, Vladimir Shevchenko, Benedetto Gianluca Siddi, Rafael Silva Coutinho, Luiz Gustavo Silva de Oliveira, Gabriele Simi, Saverio Simone, Marek Sirendi, Nicola Skidmore, Tomasz Skwarnicki, Eluned Smith, Iwan Thomas Smith, Jackson Smith, Mark Smith, Lais Soares Lavra, Michael Sokoloff, Paul Soler, Bruno Souza De Paula, Bernhard Spaan, Patrick Spradlin, Srikanth Sridharan, Federico Stagni, Marian Stahl, Sascha Stahl, Pavol Stefko, Slavomira Stefkova, Olaf Steinkamp, Simon Stemmle, Oleg Stenyakin, Holger Stevens, Sabin Stoica, Sheldon Stone, Barbara Storaci, Simone Stracka, Maria Elena Stramaglia, Mihai Straticiuc, Ulrich Straumann, Liang Sun, William Sutcliffe, Krzysztof Swientek, Vasileios Syropoulos, Marek Szczekowski, Tomasz Szumlak, Stephane T'Jampens, Andrey Tayduganov, Tobias Tekampe, Giulia Tellarini, Frederic Teubert, Eric Thomas, Jeroen van Tilburg, Matthew James Tilley, Vincent Tisserand, Mark Tobin, Siim Tolk, Luca Tomassetti, Diego Tonelli, Stig Topp-Joergensen, Francis Toriello, Rafael Tourinho Jadallah Aoude, Edwige Tournefier, Stephane Tourneur, Karim Trabelsi, Murdo Traill, Minh Tâćm Tran, Marco Tresch, Ana Trisovic, Andrei Tsaregorodtsev, Panagiotis Tsopelas, Alison Tully, Niels Tuning, Artur Ukleja, Andrey Ustyuzhanin, Ulrich Uwer, Claudia Vacca, Vincenzo Vagnoni, Andrea Valassi, Sebastien Valat, Giovanni Valenti, Maarten Van Dijk, Ricardo Vazquez Gomez, Pablo Vazquez Regueiro, Stefania Vecchi, Maarten van Veghel, Jaap Velthuis, Michele Veltri, Giovanni Veneziano, Aravindhan Venkateswaran, Tobias Anton Verlage, Maxime Vernet, Mika Vesterinen, Joao Vitor Viana Barbosa, Benoit Viaud, Daniel Vieira, Maria Vieites Diaz, Harald Viemann, Xavier Vilasis-Cardona, Marcela Vitti, Vladimir Volkov, Achim Vollhardt, Balazs Voneki, Alexey Vorobyev, Vitaly Vorobyev, Christian Voß, Jacco de Vries, Carlos Vázquez Sierra, Roland Waldi, Charlotte Wallace, Ronan Wallace, John Walsh, Jianchun Wang, David Ward, Heather Mckenzie Wark, Nigel Watson, David Websdale, Andreas Weiden, Mark Whitehead, Jean Wicht, Guy Wilkinson, Michael Wilkinson, Mark Richard James Williams, Matthew Williams, Mike Williams, Tim-

othy Williams, Fergus Wilson, Jack Wimberley, Michael Andreas Winn, Julian Wishahi, Wojciech Wislicki, Mariusz Witek, Guy Wormser, Stephen Wotton, Kenneth Wraight, Kenneth Wyllie, Yuehong Xie, Zhou Xing, Zhirui Xu, Zhenwei Yang, Zishuo Yang, Yuezhe Yao, Hang Yin, Jiesheng Yu, Xuhao Yuan, Oleg Yushchenko, Kristian Alexander Zarebski, Mikhail Zavertyaev, Liming Zhang, Yanxi Zhang, Alexey Zhelezov, Yangheng Zheng, Xianglei Zhu, Valery Zhukov, and Stefano Zucchelli. Expression of Interest for a Phase-II LHCb Upgrade: Opportunities in flavour physics, and beyond, in the HL-LHC era. Technical Report CERN-LHCC-2017-003, CERN, Geneva, Feb 2017.

[2] Niloufar Alipour Tehrani, Samir Arfaoui, Mathieu Benoit, Damiano Celeste, Dominik Dannheim, Florentina Pfleger, and Sophie Redford. Calibration of ultra-thin hybrid pixel detector assemblies with Timepix readout ASICs. Sep 2015.

[3] M. Benoit et al. Testbeam results of irradiated ams H18 HV-CMOS pixel sensor prototypes. 2016, 1611.02669.

[4] Andy Buckley. The hepthesis LaTeX class.

[5] A Dominguez, D Abbaneo, K Arndt, N Bacchetta, A Ball, E Bartz, W Bertl, G M Bilei, G Bolla, H W K Cheung, M Chertok, S Costa, N Demaria, Daniel Dominguez Vazquez, K Ecklund, W Erdmann, K Gill, G Hall, K Harder, F Hartmann, R Horisberger, W Johns, H C Kaestli, K Klein, D Kotlinski, S Kwan, M Pesaresi, H Postema, T Rohe, C SchÃd'fer, A Starodumov, S Streuli, A Tricomi, P Tropea, J Troska, F Vasey, and W Zeuner. CMS Technical Design Report for the Pixel Detector Upgrade. Technical Report CERN-LHCC-2012-016. CMS-TDR-11, Sep 2012. Additional contacts: Jeffrey Spalding, Fermilab, Jeffrey.Spalding@cern.ch Didier Contardo, Universite Claude Bernard-Lyon I, didier.claude.contardo@cern.ch.

[6] I Rubinskiy. An EUDET/AIDA Pixel Beam Telescope for Detector Development. (AIDA-CONF-2015-035), Jun 2011.

List of figures

List of tables